Journal of Marine Science and Engineering

MDPI

Article

When Does a Light Sphere Break Ice Plate Most by Using Its Net Buoyance?

Bao-Yu Ni [1,*], Hao Tan [1], Shao-Cheng Di [1], Chen-Xi Zhang [1], Zhiyuan Li [2], Luofeng Huang [3] and Yan-Zhuo Xue [1]

[1] College of Shipbuilding Engineering, Harbin Engineering University, Harbin 150001, China
[2] Department of Mechanics and Maritime Sciences, Chalmers University of Technology, SE-41296 Gothenburg, Sweden
[3] School of Water, Energy and Environment, Cranfield University, Cranfield MK43 0AL, UK
* Correspondence: nibaoyu@hrbeu.edu.cn

Abstract: A free-rising buoyant sphere can break an ice plate floating above it. The problem is when the light sphere breaks the ice plate most, or the optimal relative density of the sphere which can break the ice plate the most severely. This experimental study was done to answer this problem. A set of experimental devices were designed, and a high-speed camera system was adopted to record the whole dynamic process, including the free-rising of the sphere, the collision between the sphere and the ice plate, the crack initiation and propagation, as well as the breakup of the ice plate. The failure mode of the ice plate under impact load was analyzed. It was found that conical cracks were formed under the reflected tensile wave at the top surface of the ice plate. On this basis, the influences of ice thickness, the initial submergence depth, and the relative density of the sphere on ice-breaking were further investigated. An optimal relative density of the sphere was found when the sphere was released at a certain initial submergence depth, at which point the ice was damaged the most severely. For example, when the dimensionless initial submergence depth of the sphere was 2.31, the optimal relative density of the sphere was close to 0.4, with the probability of the ice plate breakup as high as 91.7%. It was also found from the experiments that the degree of damage to the ice plate correlated well with the kinetic energy of the sphere just before collision. Results showed that the optimal relative density can be estimated by theoretical analysis of the kinetic energy of the sphere, which will provide a reference for potential icebreaking applications in the future.

Keywords: icebreaking; free-rising; buoyant sphere; impact load; experimental study

Citation: Ni, B.-Y.; Tan, H.; Di, S.-C.; Zhang, C.-X.; Li, Z.; Huang, L.; Xue, Y.-Z. When Does a Light Sphere Break Ice Plate Most by Using Its Net Buoyance? *J. Mar. Sci. Eng.* **2023**, *11*, 289. https://doi.org/10.3390/jmse11020289

Academic Editor: Eva Loukogeorgaki

Received: 31 December 2022
Revised: 18 January 2023
Accepted: 20 January 2023
Published: 29 January 2023

Copyright: © 2023 by the authors. Licensee MDPI, Basel, Switzerland. This article is an open access article distributed under the terms and conditions of the Creative Commons Attribution (CC BY) license (https://creativecommons.org/licenses/by/4.0/).

1. Introduction

The Arctic climate warming [1,2] has increased the frequency of human activities in this area. In order to expand the scope of activities in the Arctic and realize Arctic year-round navigation [3], icebreaking is a crucial technology [4]. Since the first true modern sea-going icebreaker Yermak [5], human beings have been using icebreakers for icebreaking operation in polar regions for more than one hundred years, and researchers are still working on them [6–9]. In addition to using icebreakers, some researchers are also trying to find new methods of breaking ice, including moving loads by virtue of flexural-gravity waves [10–12], high-pressure bubble [13,14] and high-speed water jet [15] etc. On the other hand, ice can also be broken under the impact vertically. Many scholars have also studied ice-breaking in the vertical direction. Ye et al. [16] simulated a submarine surfacing through the ice under a given constant speed by using the peridynamics method. However, for most underwater bodies, constant speed is difficult to control and the ice needs to be broken by net buoyance in many cases. For example, a bowhead whale needs to break the ice sheet above it for ventilation and it can break an ice sheet up to 60 cm thick by buoyance [17]. Therefore, this paper explored when a light sphere breaks ice plate the

most by using its net buoyance, or the optimal relative density of the sphere which can break the ice plate the most severely.

Before studying this problem, there were several aspects to be introduced: first, the damage criteria of ice plates under vertical loads, including static/quasi-static loads and dynamic loads; second, methods to measure or judge the damage degree of impact between bodies; third, relevant work on the collision of bodies and ice sheet along the vertical direction. Then, we expanded the literature review from these three aspects.

First, the damage criteria of ice plates under vertical loads were reviewed. Static/quasi-static loads can be divided into concentrated and distributed loads, according to the ratio of contact area relative to ice thickness [18]. Various criteria have been proposed for predicting the breakup of an ice sheet. The most common one is the stress criterion, which can be obtained by the elastic analysis for the instantaneous loading case, and this method was developed significantly by Kerr [19]. However, when the load at the moment of impact was difficult to obtain or measure, some scholars, e.g., Shapiro [20], proposed that breakthrough occurs when critical deflection is reached, regardless of creep before failure, which was also named as deflection and strain criteria. The critical strain-energy per unit volume concept is also used extensively in strength-of-materials literature [21]. The advantage of the strain energy criterion relies on the fact it takes the loading and strain history into account. On these bases, Assur [22] and Frankenstein [23] studied the sequence of failure of an ice cover under static concentrated and distributed loads vertically downwards. There are usually three stages: the first is a radial crack on the bottom of the ice plate as a result of significant bending moments; the second is a circumferential crack on the top of the ice plate at some distance away from the load; the third is the breakup of ice plate along the radial and innermost circumferential cracks. The fracture stages are classical for ice plates subject to vertical loading.

In addition to static or quasi-static loads, impact load is another type of icebreaking load. Different from static or quasi-static loads, various shockwaves are observed in the ice at the instant of load impacting the ice. For example, when a high-speed water jet impacts an ice plate [15], the shock wave propagates in the form of volume waves (including longitudinal waves and transverse waves) in the plate and propagates in the form of Rayleigh surface waves on the surface of the plate [24]. Longitudinal waves are compression waves before being reflected by the lower surface of the plate and become expansion waves due to the acoustic impedance of the different media on both sides of the interface. Transverse waves are shear waves. Rayleigh surface waves have vertical and horizontal components that correspondingly induce tensile and shear stresses. The propagation and interaction of shockwaves may be a fundamental cause of crack formation and propagation [25].

Second, methods to measure or judge the damage degree of impact between bodies are always challenging in experiments. On the one hand, researchers tried to explore contact measurements to study impact. Bouzid et al. [26] concerned a glass plate subject to impact at different loading rates by using two experiments: a compression split Hopkinson pressure bar, and the normalized drop ball test. The pulse was obtained by the gauges attached on the back of the glass sample. For studying the tensile strength of ice subjected to dynamic loading, Zhang et.al [27] investigated the dynamic tensile behaviors of distilled-water and river-water ice by a modified split Hopkinson pressure bar system.

However, in most cases, it is very hard to obtain data through contact measurement. Non-contact measurements and analysis were also adopted. Woodward et al. [28] studied the damage of brittle materials with different rigidity caused by projectiles of different diameters, in which the kinetic energies of the projectiles and the debris were recorded and analyzed. Dooge et al. [29] used ice particles with different mass and velocity to impact the aluminum plate in the experiment and made qualitative and quantitative analysis of the damage. They found that the incident kinetic energy of the ice ball had a good correlation with the expected damage of the aluminum plate. Kim et al. [30] investigated the damage resistance of thin-walled composite structures to ice impact by experiment, and

one of the experiments was performed on a dynamic force measurement device. The experimental results showed a linear relationship between the measured peak force and the kinetic energy of the projectile, regardless of the projectile size. Some authors [31–33] have also studied the impact of ice ball on a rigid plate from experimental and numerical ways. One of the main conclusions was that microstructure of ice did not play an important role under these conditions and there was a correlation between impact force and kinetic energy. By contrast, some authors put forward different opinions on the study of impact. Xue et al. [34] studied the response of glass under dynamic impact load by using the drop ball test and proposed that the energy threshold was not specified as a prediction index, which did not take the time spent in contact during the impact event into account. Therefore, a metric for impact testing based on a momentum change threshold was established, and it was found that the momentum change had a linear relationship with the maximum deformation of the glass. They concluded that the momentum change was more suitable for predicting the maximum deformation. There are also some other problems concerning impact, such as dynamic compaction. Knut et al. [35] conducted field and laboratory experiments, respectively, to explore the influence of momentum and energy on the performance of dynamic compaction technologies. It was found that kinetic energy had no obvious effect on the crater depth. For an inelastic compaction process, they concluded that the momentum rather than energy determined the depth of the crater.

It can be seen from the above that there is always a controversy whether kinetic energy or momentum dominates the damage degree of impact between bodies [28–35]. For the collision between ice plate and a buoyant sphere, it will become more complex, as it is still difficult to define the damage degree of ice plate.

Third, there is relevant work on the collision of bodies and ice sheet along vertical direction. Kozlov [36] studied the collision between a rigid sphere with a high initial speed and a very thick ice on water. He found that after the first collision with the ice plate, the maximum value of the sphere's intrusion at a certain point in time depended on its own kinetic energy before impact. Orlov and Bogomolov [37] quantitatively described the process of large impactors penetrating ice in the initial range below the speed of sound in air. It was found that the increase in crater depth was directly proportional to the impact velocity. The volume of ice destroyed was insignificant. Ren and Zhao [38] studied the process of a sphere falling from the top of an ice plate, breaking ice before entering water. Attention was paid to the numerical modelling of the interaction of ice, water and sphere. Wang et al. [39] simulated the process of an underwater cylinder breaking ice vertically before exiting water. The collision direction of this work was also from bottom to top, but the motion of the cylinder was prescribed, rather than free rising.

It can be seen that most previous work on the collision of a body and ice along vertical direction either concerned the intrusion of the sphere into the thick ice, or the damage of ice under the body with a prescribed velocity. To the best of our knowledge, no research on icebreaking by a free-rising buoyant sphere has been published. Many interesting problems are involved in the icebreaking process under such an icebreaking scenario. When does a light sphere break ice plate most by using its net buoyance? How can we define the damage degree in experiments? Does kinetic energy or momentum dominate the damage degree of ice plate? All these problems formed the main motivation and innovation of this paper. The paper studied the icebreaking process of a free-rising light sphere with variable weight in experiments. The whole process of the motion of sphere and the response of the ice plate was recorded and analyzed. On the basis of the experimental results, some simplified theoretical approaches were also adopted to find an explicit expression of the optimal relative density of the sphere. The results may provide potential applications in guiding an underwater vehicle that navigates under the ice sheet and needs to break ice by net buoyance in case of a mission or an emergency.

2. Theory

Driven by the buoyant force, a light sphere starts to accelerate from a resting position under the ice plate until it collides with the ice plate. A sketch of the problem with variables is presented in Figure 1. The definition of variables is as follows: D is the diameter of the sphere; L_0 is the initial submergence depth, which is the distance between the center of the sphere and the bottom surface of the ice plate while the sphere is stationary; h is the thickness of the ice plate; ρ_s is the density of the sphere; ρ_w is the density of water; g is the acceleration of gravity; U is the velocity of the sphere.

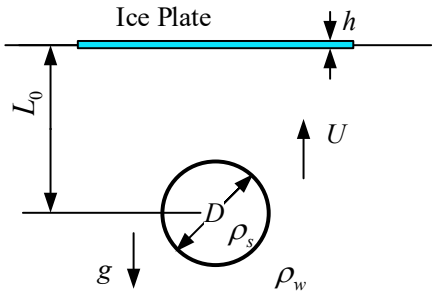

Figure 1. Sketch of the problem.

The ascension of a rising buoyant sphere is modeled with a simple theoretical force balance illustrated in Figure 2 and demonstrated as follows [40]:

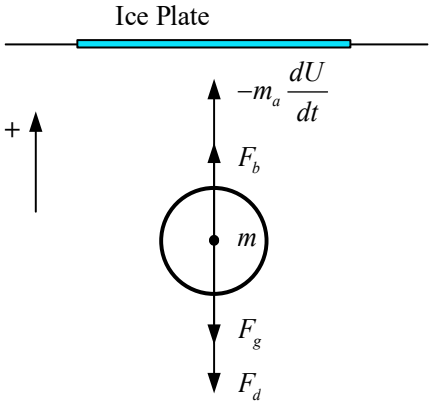

Figure 2. Free body diagram of a rising buoyant sphere.

$$(m + m_a)\frac{dU}{dt} = F_b - F_g - F_d, \tag{1}$$

where $m = \rho_s V$ is the mass of the sphere, where $V = \frac{4}{3}\pi\left(\frac{D}{2}\right)^3$ is the volume of the sphere; $m_a = C_m \rho_w V$ is the added mass of the sphere and C_m is the added-mass coefficient; $F_b = \rho_w g V$ is the buoyant force; $F_g = \rho_s g V$ is the gravity force; $F_d = \frac{1}{2}\rho_w U^2 C_d A$ is the drag force, where $A = \pi\left(\frac{D}{2}\right)^2$ is the cross-sectional area and C_d is the drag coefficient. It is remarkable that C_m is concerned with the distance between boundary to the sphere [37–39].

To facilitate unified expression, Equation (1) is rewritten as follows:

$$(m+m_a)\frac{dU}{dx}\cdot\frac{dx}{dt}=F_b-F_g-F_d, \tag{2a}$$

$$U\frac{dU}{dx}=\frac{-3C_d\cdot U^2+4Dg\left(1-\bar{\rho}\right)}{4D\left(\bar{\rho}+C_m\right)}. \tag{2b}$$

In Equation (2a) and Equation (2b), x is the displacement of the rising buoyant sphere; $\bar{\rho}=\frac{\rho_s}{\rho_w}$ is the dimensionless density of the sphere. When the sphere moves in an unbounded fluid, C_m is equal to 0.5. However, when the sphere approaches to the wall vertically, the expression of C_m changes with the distance to the wall. Many researchers studied the variation law of C_m with wall [41,42] and Kharlamov et al. [43] provided a fitting formula of C_m of a sphere approaching to a rigid wall vertically with a maximum deviation from the computed data 4×10^{-3}:

$$C_m=0.5+H_1\bar{l}^{t_1}+H_2\bar{l}^{t_2}, \tag{3}$$

where $\bar{l}=\left(\frac{L_0-x}{D}\right)$ is a dimensionless distance between the center of the sphere and the wall, and constants $H_1=0.2182$, $t_1=-3.21$; $H_2=0.081$, $t_2=-19$.

If one assumes C_m as 0.5 and C_d as a constant during the movement, Equation (2) can be rewritten as follow:

$$U\frac{dU}{dx}=-\frac{3C_d}{2D\left(1+2\bar{\rho}\right)}U^2+\frac{2g\left(1-\bar{\rho}\right)}{\left(1+2\bar{\rho}\right)}, \tag{4}$$

The general solution of Equation (4) can be written as [44]:

$$U=\left[2\int Q\cdot e^{-2\int P dx}dx+R\right]^{\frac{1}{2}}\cdot e^{\int P dx}, \tag{5}$$

where $P=-\frac{3C_d}{2D\left(1+2\bar{\rho}\right)}$, $Q=\frac{2g\left(1-\bar{\rho}\right)}{\left(1+2\bar{\rho}\right)}$, R is a constant confirmed by the initial conditions, i.e., $U=0$ when $x=0$ in the case in this paper. Therefore, R can be written as $R=\frac{Q}{P}=-\frac{4gD\left(1-\bar{\rho}\right)}{3C_d}$.

Since we are concerned with the velocity just before the sphere impacting the ice plate, the upper limit of the integral for displacement x should be $L_0-\frac{D}{2}$ right before contacting the ice plate. As a result, when the sphere contacts the ice plate, the velocity U of the sphere is

$$U_t^2=\frac{4gD\left(1-\bar{\rho}\right)}{3C_d}\left[1-e^{-\frac{3C_d}{\left(1+2\bar{\rho}\right)}\left(\bar{L}_0-\frac{1}{2}\right)}\right], \tag{6}$$

where $\bar{L}_0=\frac{L_0}{D}$ is dimensionless initial submergence depth. If one further assumes that the viscosity of the fluid can be ignored, i.e., $C_d=0$.

Equation (4) can be simplified further as:

$$U\frac{dU}{dx}=\frac{2g\left(1-\bar{\rho}\right)}{\left(1+2\bar{\rho}\right)}. \tag{7}$$

One can easily get the velocity U of the sphere when it contacts the ice plate as

$$U_t^2=\frac{4gD\left(1-\bar{\rho}\right)}{\left(1+2\bar{\rho}\right)}\left(\bar{L}_0-\frac{1}{2}\right). \tag{8}$$

Then in the nondimensionalized system, the following three parameters are chosen as the characteristic quantities: diameter of the sphere D, water density ρ_w and gravitational acceleration g.

3. Experimental Methods

3.1. Ice Specimen Preparation

From the perspective of ice mechanics, ice can be regarded as one of the most complex materials in nature [45–47]. Ice in nature contains many defects, including preexisting cracks, inclusions, pores, grain boundaries, etc. [48,49] which further aggravates the uncertainty of the experiment. Therefore, some researchers [50–52] proposed using freshwater as the material to prepare experimental ice in the laboratory. Figure 3 shows a schematic diagram of the freshwater ice plate preparation method. The ice plates in this study were made by freshwater in a cryostat at −20 °C. The freshwater was boiled in order to maximize the removal of dissolved air in the water and to avoid the presence of bubbles. The boiled fresh water was placed in a cylindrical container without a top cover. The container was made of expanded polystyrene (EPS), whose good adiabatic properties ensure that the heat transfer direction was from top to bottom, in the same way as the growth direction of the ice crystal in reality. When the requirements of the thickness of the ice plates were met, the ice plates were removed from the container and moved into a cryostat at −5 °C for 10 h, which was to prevent the ice plate from breaking due to the excessive temperature difference between the ice plate and water [15,53]. Figure 4 shows a picture of the ice plate samples. The diameter of ice plates was 345 mm, and the thicknesses were 6 mm, 8 mm, and 10 mm, respectively. The mechanical properties of the ice plate were obtained by testing at −5 °C. The average value of Young's modulus of ice was 6.2 GPa, and the average compressive and flexural strengths of ice were 9.4 MPa and 2.4 MPa, respectively. The rest of the properties can be found in Ni et al. [53].

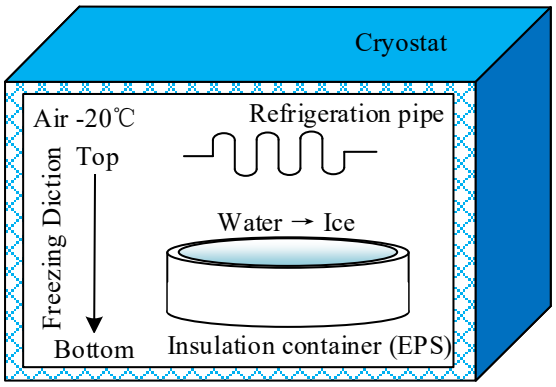

Figure 3. Schematic diagram of ice-making in the cryostat.

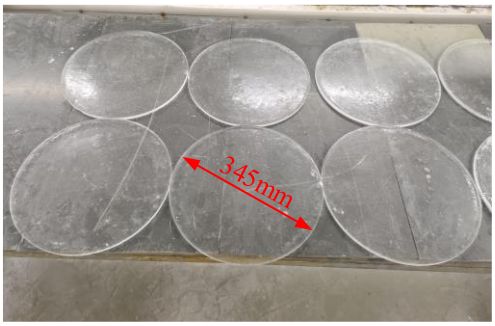

Figure 4. Ice plate samples.

3.2. Experimental Setup

Figure 5 shows the experimental setup. The experimental setup can be divided into four systems: (1) the sphere location and releasing system; (2) the fixing system; (3) the supporting system; (4) the camera system.

The sphere location and releasing system included a lift platform (in blue) and a releasing device (in yellow), as shown in Figure 5a,b. The former was placed in the center of the bottom of the tank, which was used to manipulate the initial submergence depth of the sphere below the ice plate. The latter was placed above the lift platform and adopted an electromagnet to control the release of the sphere. Finally, the light sphere with an iron button was placed on the releasing device. The sphere was made of poly lactic acid (PLA) using 3D printing and painted with black nitrocellulose lacquer. Its diameter was 112.5 mm. The size of the sphere was determined by the size of water tank. The weight of the sphere was variable by using different ballasts inside it, so the relative density of the sphere was achieved easily in the experiment.

The fixing system was adopted to restrict the motion of the ice plate on the free surface. We tried to simulate the collision of a sphere with a very large ice sheet, rather than a free-floating ice. However, due to the limitation of ice-making technology and experimental equipment, the size of the ice plate could not be very large. Considering that the displacement and ration angle of the ice sheet tend to be zero at a very large distance, we designed a fixing system to rigid fix the edge of the ice plate. The main body of the fixing system was a supporter made of polymethyl methacrylate (PMMA). The supporter had a groove with diameters of 345 mm and 325 mm, as shown in Figure 5c. During the experiment, the ice plate was first put into the groove of the supporter, and then the fixed ring was covered over the ice plate, as shown in the enlarged view of Figure 5c, and finally, the fixed ring was fixed with the supporter by four Clamps2. Under the joint constraint of supporter and fixed ring, the boundary condition of the ice plate was completely fixed. The ice fixing system was fixed with the water tank by eight Clamps1.

The supporting system consisted of a square water tank and an outside shell frame. The water tank was made of transparent glass, and its principal dimension was 0.6 m in length.

The camera system included two high-speed cameras and four LED lamps. One camera was a PHANTOM VEO-640S (Phantom/AMETEK, USA), placed on the horizontal surface with the resolution rate of 1024 × 1024, which captured photos at 10,000 frames per second. The other was a PHOTRON Fastcam Mini A1300 (Photron,Japan), placed on the vertical surface with the resolution rate of 768 × 528, which captured photos at 1000 frames per second. Camera 1 was in charge of capturing the motion trajectory of the floating sphere. The velocity and corresponding kinetic energy of the sphere were obtained by image recognition technology. Meanwhile, the destruction of the ice plate was captured by Camera 2. By sending a pulse signal from Camera 1 and receiving it by the other, synchronous triggering and shooting of two cameras were achieved. Four flicker-free LED lamps were installed on the transparent water tank's side and bottom to ensure a bright shooting environment.

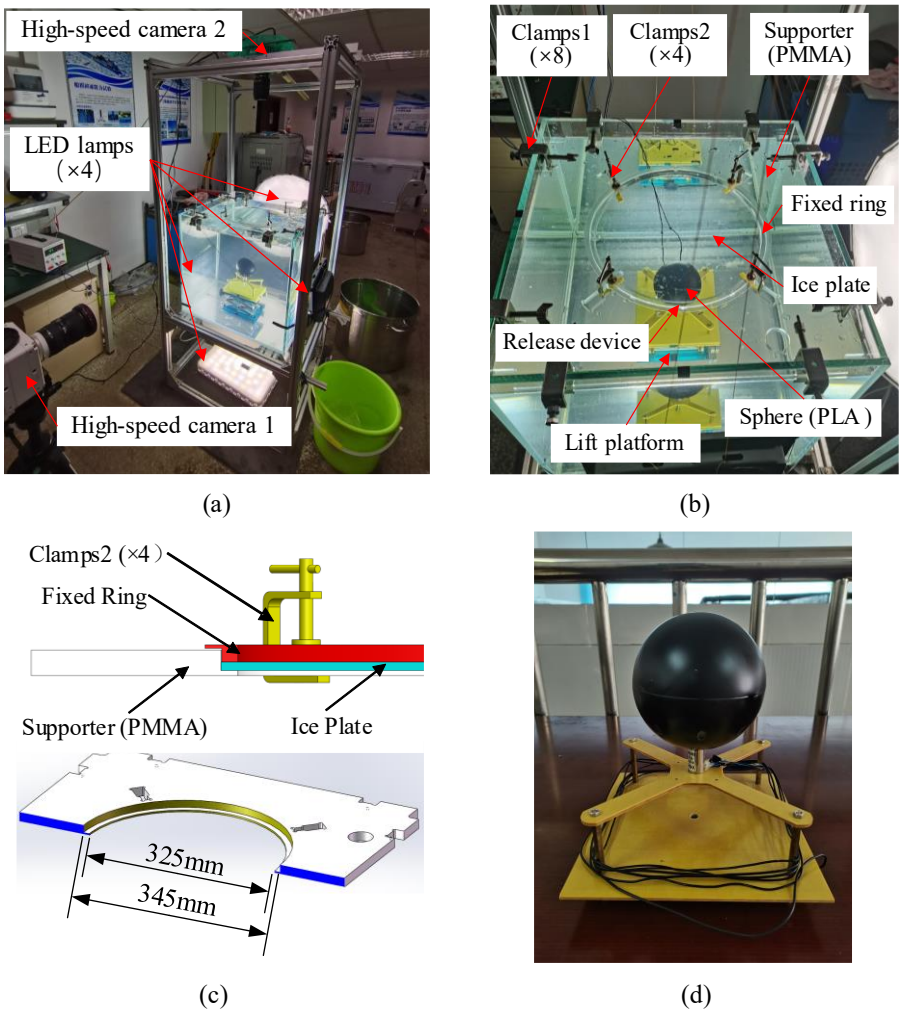

Figure 5. Experimental setup: (**a**) supporting system and camera system; (**b**) ice-fixing system and sphere location and releasing system; (**c**) cross-section diagram of ice-fixing supporter and the fixation way of the ice plate; and (**d**) releasing device and the sphere.

4. Result and Discussion

In this section, we chose a case study to analyze the icebreaking process by the buoyant sphere before discussing the influence of several parameters, including dimensionless initial submergence depth $\bar{L}_0$, dimensionless density $\bar{\rho}$ and dimensionless ice thickness $\bar{h}$.

4.1. Case Study

A case study was chosen with the following parameters: dimensionless initial submergence depth $\bar{L}_0$ was 2.31, dimensionless density $\bar{\rho}$ was 0.4 and dimensionless ice thickness $\bar{h}$ was 0.089. The movement process of the floating sphere and interactions between the sphere and the ice plate were recorded and analyzed.

Figure 6 shows curves of the velocity of the sphere along with the displacement before colliding with the ice plate. It contains: (1) initial experimental data; (2) curve obtained after filtering experimental data; (3) theoretical results with C_m = Equation (3) and $C_d = 0.44$; (4) theoretical results with $C_m = 0.5$ and $C_d = 0.44$; (5) theoretical results of Equation (8) with $C_m = 0.5$ and $C_d = 0$.

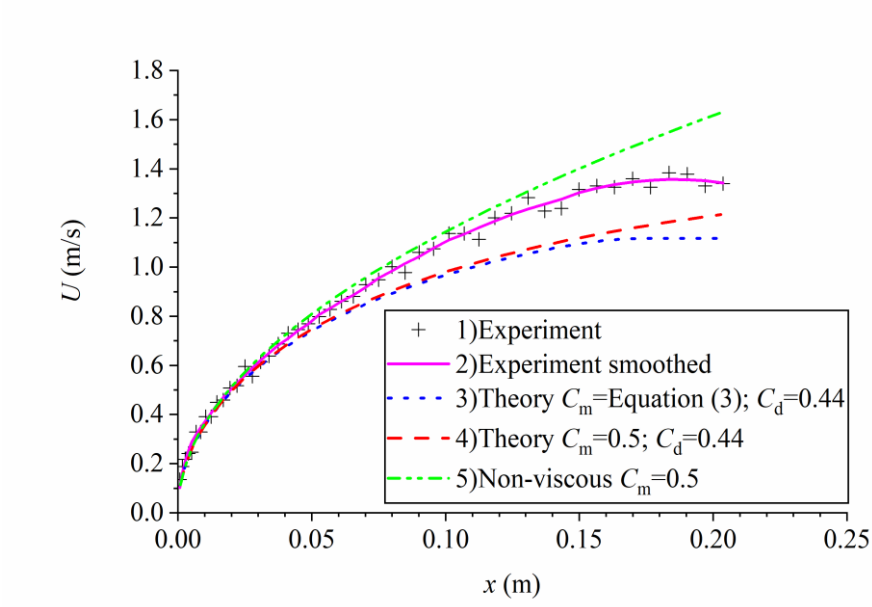

Figure 6. Variations of the velocity of the sphere along with displacement before colliding the ice plate for the case $\bar{\rho}$ = 0.4, $\bar{L}_0$ = 2.31 and $\bar{h}$ = 0.089.

According to the experiment curves (1) and (2), the sphere with zero initial velocity accelerated under the effect of net buoyant force after being released, but the acceleration amplitude gradually decreased. When the displacement of the sphere was about 0.16 m ($\bar{x}$ = 1.42) (that is, the distance from the center of the sphere to the ice plate was about 0.1 m ($\bar{l}$ = 0.89)), the velocity of the sphere was almost uniform, which indicated that the forces on the sphere were almost balanced. On the one hand, the viscous resistance increased with the velocity of the sphere. On the other hand, the additional mass force increased with the decrease of the spacing according to Equation (3). Both contributed to the balance of the net buoyant force. Therefore, in a theoretical prediction, the selections of drag and added mass coefficients C_d and C_m need to be discussed.

First, we considered the influence of added masses C_m, which was less complicated than the choice of C_d. Curves (3) and (4) showed velocities at different added mass coefficients of a sphere with and without of influence of the wall surface. When the displacement of the sphere was less than 0.16 m ($\bar{x}$ = 1.42), curves (3) and (4) overlapped basically. Beyond that, there was a deviation between two results, which denoted that the influence of wall surface should not be ignored when the sphere was very close to the wall. Once again, the comparison of curves (3) and (4) validated that the increase of added mass coefficient contributed to the balance of the sphere.

Second, the choice of C_d was particularly worth discussing. For unsteady motion, the drag coefficient C_{du} is different from the counterpart C_d at steady state. Many researchers [54–57] have carried out experimental and theoretical studies on it. For the convenience, we temporarily assumed $C_{du} = C_d$. As we know, C_d of a sphere is closely related to Re number. When $1.0 \times 10^3 < \mathrm{Re} < 2.0 \times 10^5$, C_d is around 0.44 [58–61]. Re number of the sphere in this case was mostly distributed in this interval, so the resistance coefficient was taken as 0.44 in curves (3) and (4). By comparison, $C_d = 0$ was adopted in curve (5). However, it can be seen from the comparison between curve 4) and curve (5) that the resistance coefficient of the sphere in actual motion was less than 0.44, which coincided with the researches of [62,63] on the point that C_{du} was smaller than C_d. For this reason, we decreased the resistance coefficient C_d. By trying a series of resistance coefficients, we

found that when C_d = 0.12 (as shown in Figure 7) could predict the motion of the sphere well in our cases, especially considering the influence of the wall surface on C_m.

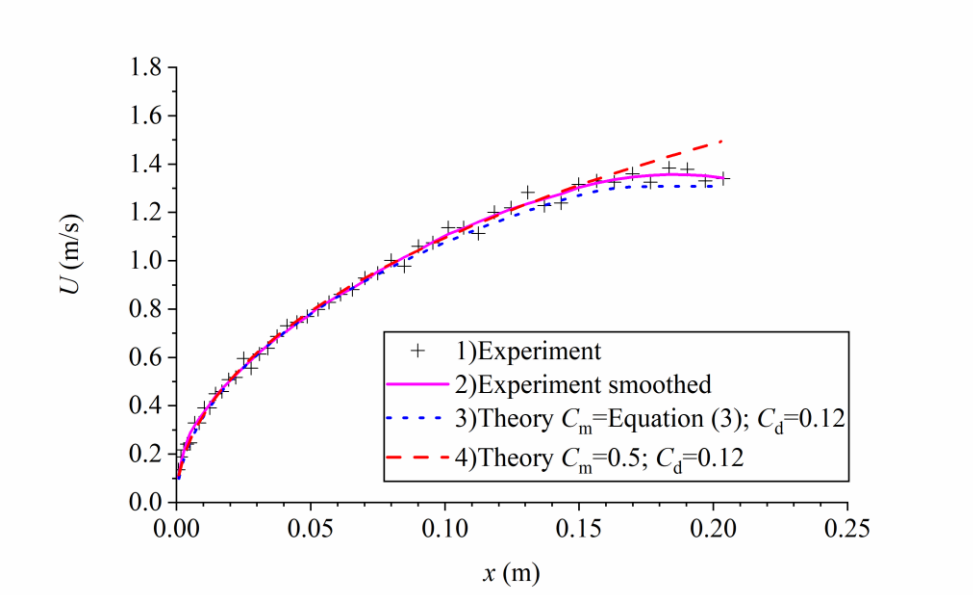

Figure 7. Displacement-velocity curves after resistance coefficient correction for the case $\bar{\rho}$ = 0.4, $\bar{L}_0$ = 2.31 and $\bar{h}$ = 0.089.

Under the acceleration process in water, as shown in Figure 6, the buoyant sphere obtained a certain velocity and started to collide with the ice plate. Figure 8 shows the typical characteristics and corresponding time during the process of the sphere impacting the ice plate until it is broken. The moment when the sphere just contacted the bottom surface of the ice plate was defined as the initial time (t' = 0 ms), as shown in Figure 8a. At the time of t' = 0.2 ms, the first radial cracks (RCs) appeared on the ice plate clearly under the collision of the sphere, shown in Figure 8b. The patterns of cracks were quite similar to those during icebreaking under distributed loads by Ashton [49]. Under the continuous loads from the buoyant sphere, radial cracks extended to the edge of the ice plate at the time of t' = 0.6 ms in Figure 8c, as marked by the red line. Figure 8d shows the formation of circumferential cracks (CCs), which were generated on the basis of RCs [26]. After generating CCs, cone cracks could be observed in the vicinity of the contacting point (stuck out by the green dotted line and partial enlarged in Figure 8e). After that, the ice plate began to break, and air entered under the ice plate through the cracks, which appeared as bubbles along the cracks in Figure 8f (stuck out by the blue dotted line). Then, cone cracks penetrated the ice plate and the debris splashed by the impact of the sphere (shown by the green circle in Figure 8g). Finally, under the action of the sphere, the wedge-shaped ice pieces in the center of the ice plate failed, and the sphere broke through the ice plate and pushed the polygonal ice fragments aside, as shown in Figure 8h. The damage process of the ice plate after impact can be summarized as follows: first, the ice plate produced RCs (RCs pattern); second, CCs were generated on the basis of RCs (RCs⊕CCs pattern); third, the ice debris splashed (debris-splashing pattern); finally, the ice plate broke up (ice-plate breakup pattern).

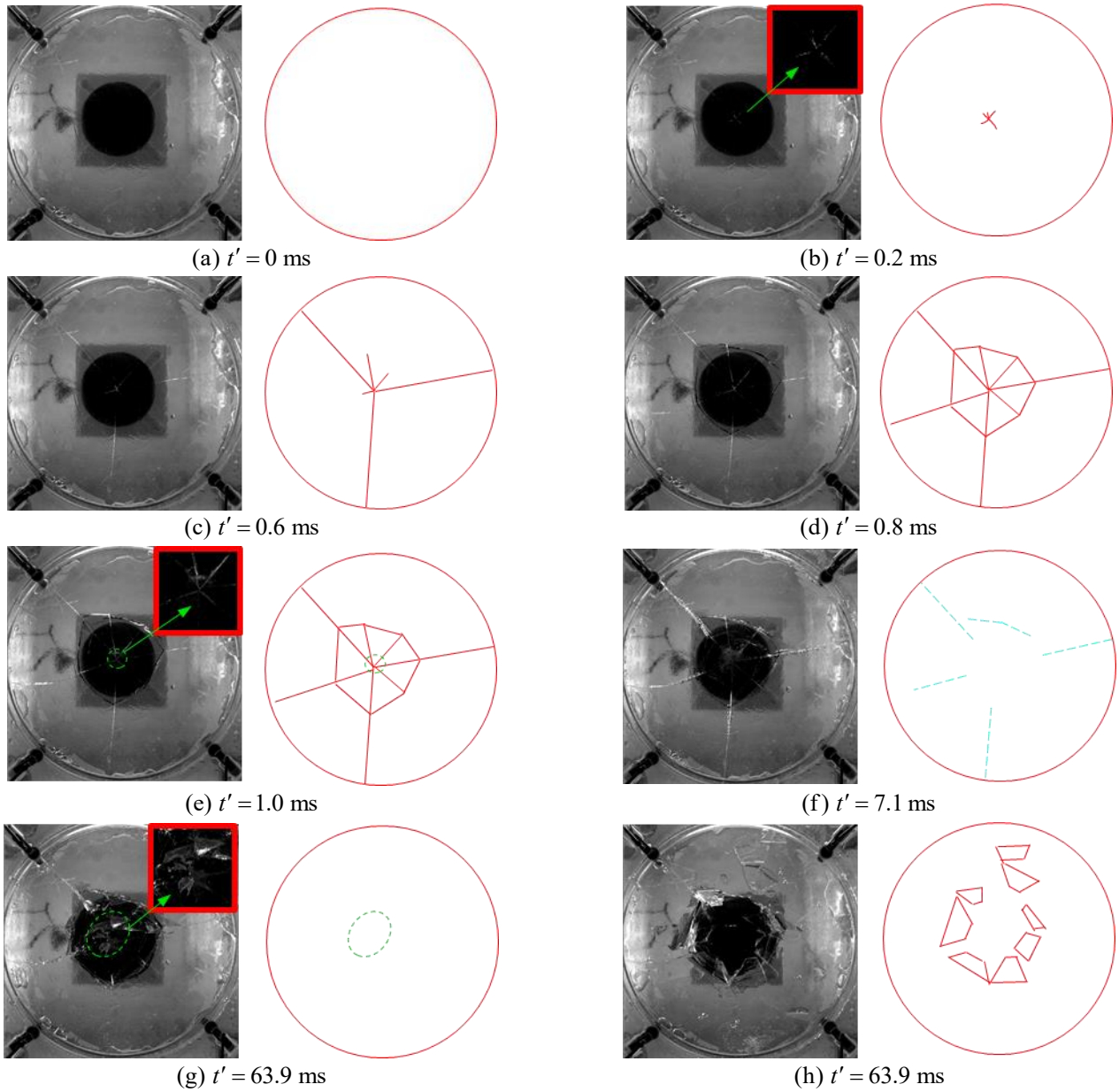

Figure 8. The breaking process of the ice plate under the impact of the buoyant sphere at different moments, as denoted in the subfigures, for the case $\bar{\rho} = 0.4$, $\bar{L}_0 = 2.31$ and $\bar{h} = 0.089$.

In order to intuitively explain the cause of the destruction of the ice plate after the impact, Figure 9 is demonstrated. As shown in Figure 9a, when the sphere collided with the ice plate, a compressive wave before a tensile wave was transmitted from the collision point. When the compressive wave arrived and was reflected by the upper surface of the ice plate, it became a tensile wave due to the acoustic impedance of the different media on both sides of the interface. Because the tensile strength of the ice (about 2.2Mpa at −5°C) is much lower than its compressive strength (about 9.4Mpa at −5°C), ice is more fragile under tensile waves compared with compressive waves [27]. Especially, when the reflected tensile waves encountered and interacted with incident tensile waves, as shown in Figure 9b, the ice plate became very fragile, as shown in Figure 9c. As a result, the ice plate broke up in spalling, leaving sloped fractures, as shown in Figure 9d. In fact, there may be more forms of wave transmission, such as shear or Rayleigh waves, whose effects complicated the destruction of the ice plate [64]. However, due to the limited shooting equipment, it was hard to record the wave propagation in ice accurately.

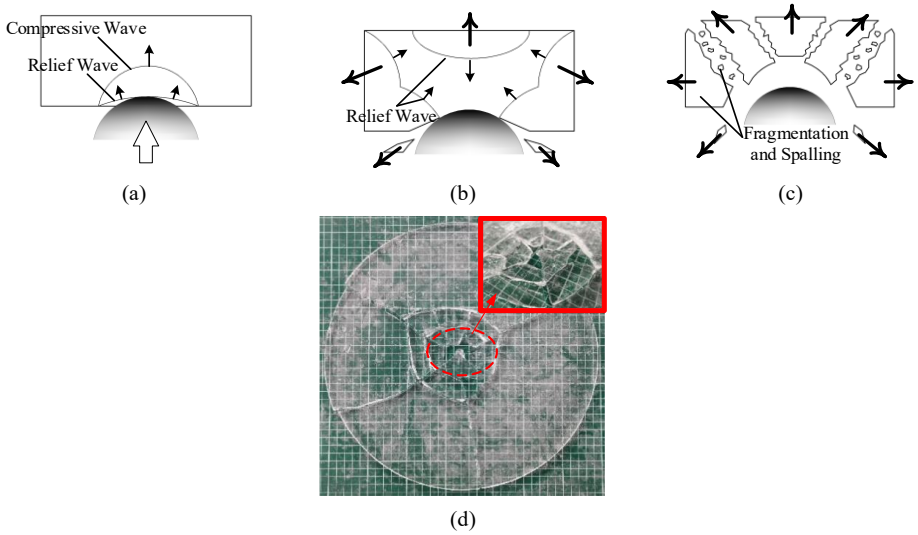

Figure 9. Schematic sequence of events in the impact, adapted from [29]: (**a**) immediately after impact, stress waves are generated; (**b**) relief waves propagate from the upper surface and fine debris splits away off; (**c**) interacting relief waves cause fragmentation and spalling; and (**d**) the broken ice plate is reassembled, and the center of the ice plates forms some sloped fractures due to the impact of the sphere.

4.2. The Effect of Dimensionless Initial Submergence Depth $\bar{L}_0$ on Ice Plate Damage

The effect of dimensionless initial submergence depth $\bar{L}_0$ was investigated by changing $\bar{L}_0$ from 0.9 to 2.31, with dimensionless ice thickness $\bar{h}$ = 0.071 and dimensionless density $\bar{\rho}$ = 0.6 constant.

Figure 10 provides the ice damage at four initial submergence depths, in which the time was all chosen at t' = 0.1 s. In Figure 10a, it can be observed that there were slight and inconspicuous RCs extending from the center of the ice plate to the edge, i.e., RCs pattern. With the increase of the initial submergence depth of the sphere, in Figure 10b, the ice was damaged severely with a greater number of RCs and several slight CCs at a distance from the center, i.e., RCs⊕CCs pattern. In Figure 10a, b), ice plates did not break up, or the cracks did not penetrate the ice plate, which was also named 'part-through' cracks [65]. In terms of the damage pattern of the ice plate, the phenomenon shown in Figure 10c was not changed significantly from that shown in Figure 10b. However, one can observe that air bubbles were captured under the ice plate, as denoted in the blue circles. This is because the cracks had penetrated the ice plate and air entered through the cracks and edges. When the initial submergence depth increased to 2.31, as shown in Figure 10d, in addition to RCs and CCs on the ice plate, ice debris can be clearly found splashing from the center of the ice plate, i.e., a debris-splashing pattern.

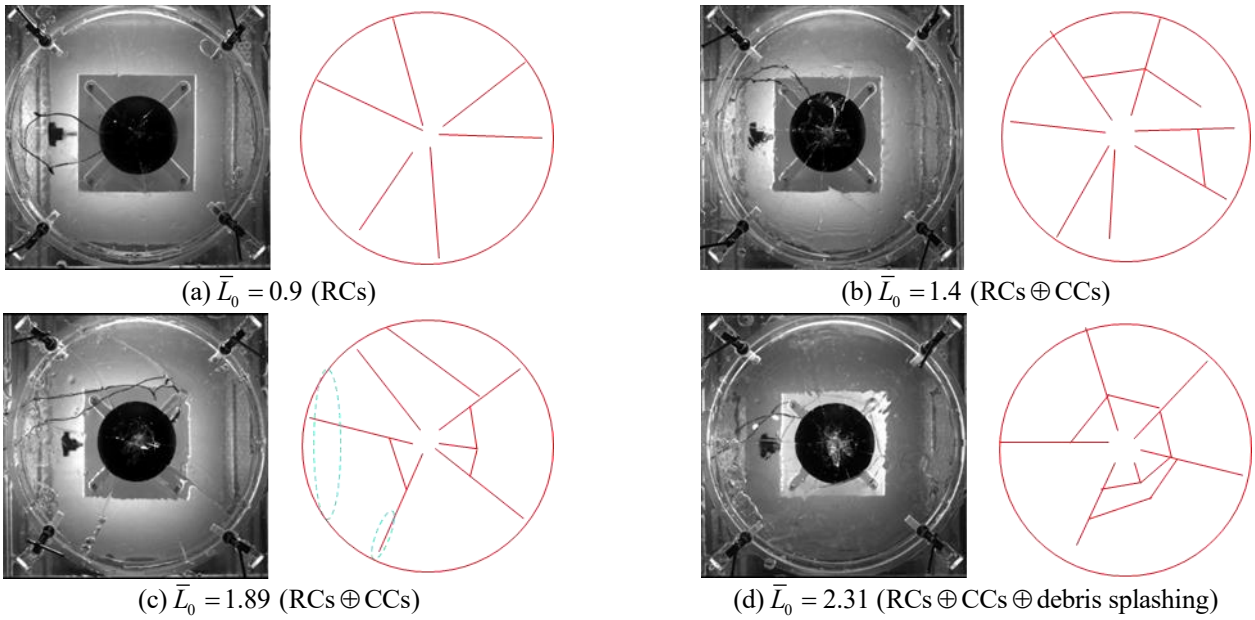

Figure 10. Typical damage patterns of ice plates with different $\bar{L}_0$, as denoted in the subfigures, with the initial condition of $\bar{\rho} = 0.6$ and $\bar{h} = 0.071$ at $t' = 0.1$ s.

As mentioned in the previous section, affecting by the nature of the ice plate, we cannot obtain the strain of the ice plate during the collision directly by using contact measurement methods, such as strain gauges attached to the surface of the ice plate. For this reason, we adopted an indirect method to describe the damage degree of the ice plate as above. For the condition in this section, it is common to expect the result before the experiment, i.e., that within a certain range (will be discussed in Section 4.4), the greater the initial submergence depth of the sphere is, the more severely the ice plate is damaged. Experimental results validated this expectation. Therefore, we can predict that the damage degree of the ice plate becomes more severe from "RCs" to "RCs⊕CCs" and then to "splashing".

4.3. The Effect of Dimensionless Ice Thickness $\bar{h}$ on Ice Plate Damage

On the basis of Figure 10 in Section 4.2, the effect of ice thickness was further investigated by changing $\bar{h}$ from 0.053 to 0.089, with $\bar{L}_0 = 2.31$ and $\bar{\rho} = 0.6$ constant.

In the case of $\bar{h} = 0.089$, both radial and circumferential cracks (namely RCs⊕CCs pattern) can be observed (Figure 11a). When the dimensionless ice thickness decreased to 0.071, not only were RCs and CCs observed in the ice plate, but debris splashing was found in Figure 11b, which showed a debris-splashing damage pattern. With the decrease of dimensionless thickness to 0.053, the damage to the ice plate became quite serious. The sphere broke up the ice plate into multiple triangular and quadrilateral pieces and the number of ice debris became larger, as shown by the green circle in Figure 11c, presenting an ice plate-breakup pattern.

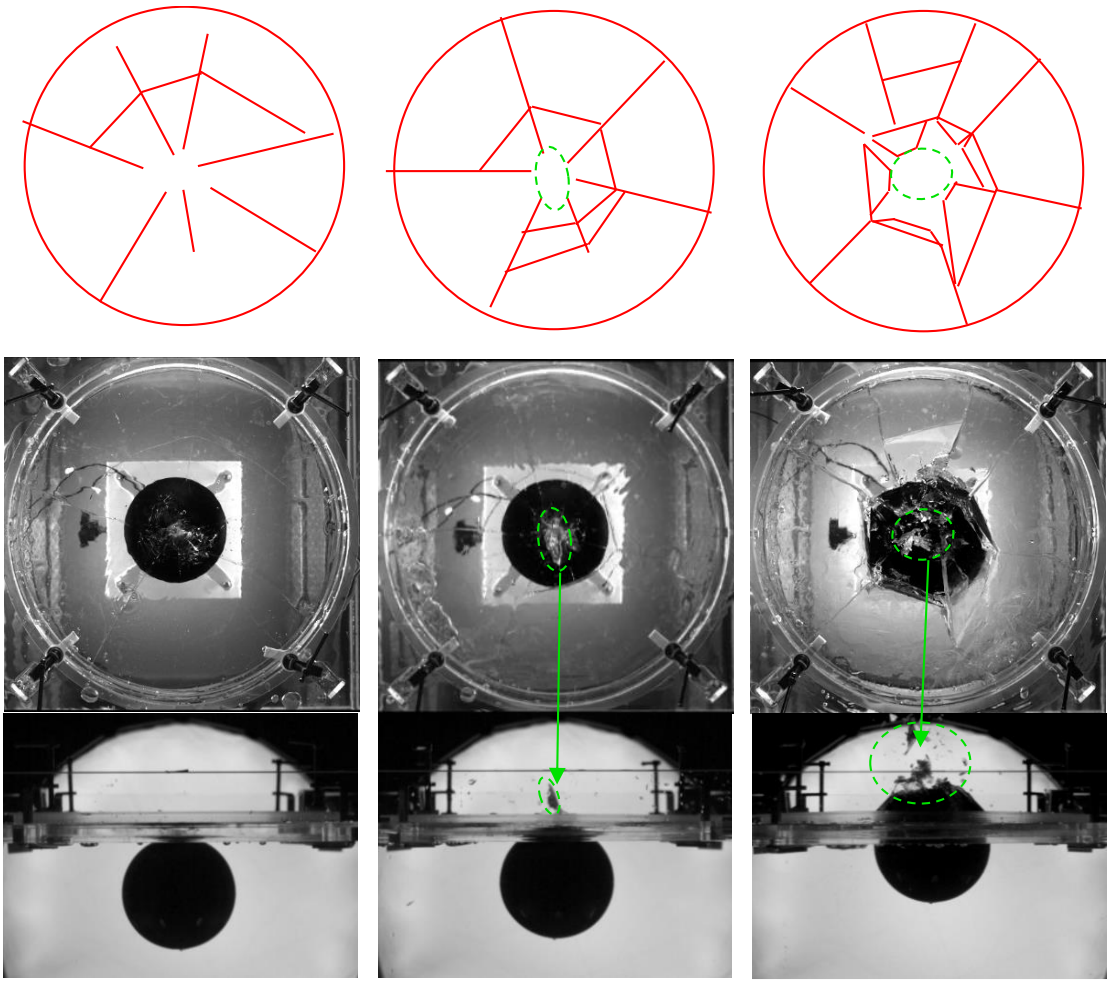

(a) $\bar{h} = 0.089$ (b) $\bar{h} = 0.071$ (c) $\bar{h} = 0.053$

Figure 11. Typical damage patterns of ice plates with different dimensionless thickness $\bar{h}$ with the initial condition of $\bar{\rho}$ = 0.6 and $\bar{L}_0$ = 2.31 when t' = 0.1 s. (upper photos are captured a from bird's eye view by Camera 2 and lower ones are captured from a horizontal perspective by Camera 1).

Figure 12 displays final equilibrium positions of the sphere after resting. By comparison, it can be found that although the sphere did not break through the ice plate in Figure 12a,b, the final submergence depth was different. l_1 was larger than l_2 a bit, while l_1 and l_2 were both larger than l_3 distinctly. This can be expected as the thinner the ice plate was, the damage the ice plate became more severe. The damage to the ice plate, including debris and hole, provided space for the sphere to rise.

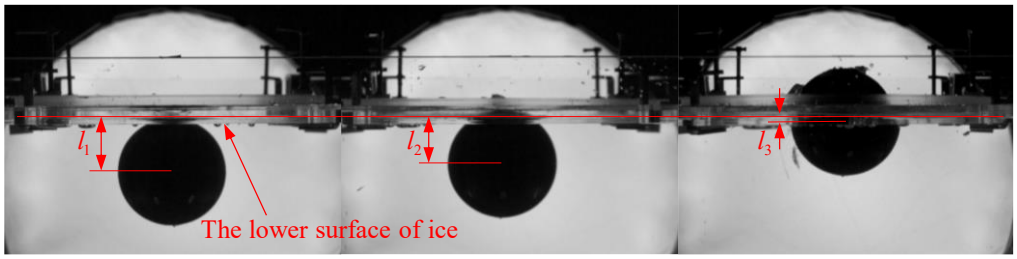

(a) $\bar{h} = 0.089$ (b) $\bar{h} = 0.071$ (c) $\bar{h} = 0.053$

Figure 12. Equilibrium positions of the sphere after colliding with the ice plate at different $\bar{h}$, as denoted in the subfigures, with $\bar{\rho}$ = 0.6 and $\bar{L}_0$ = 2.31.

Similar to Section 4.3, it is common to expect the result before the experiment, i.e., the thinner the ice plate was, the more severely it was damaged by the sphere with the same submergence depth and relative density. Experimental results validated this expectation. Therefore, we can show that the damage degree of the ice plate becomes more severe from "'RCs⊕CCs" to "splashing" and then to "breakup". Together with Section 4.3, we can ascertain that the pattern is becoming worse from "RCs" to "breakup", which will lay a foundation for judging the damage degree of the ice plate hereinafter.

4.4. The Effect of Dimensionless Density $\bar{\rho}$ on Ice Plate Damage

This section explores the effect of dimensionless density $\bar{\rho}$ on ice plate damage. Spheres with different dimensionless densities were used to break the ice plate with $\bar{h}$ = 0.089 and $\bar{L}_0$ = 2.31 constant.

Figures 13–15 represent the dimensionless velocity, dimensionless kinetic energy, and dimensionless momentum of spheres with different relative densities at the moment of contact with the ice plate. There are three curves in each figure, representing the experimental value, theoretical predicted values with C_m = Equation (3); C_d = 0.12 and C_m = 0.5; C_d = 0.12, respectively. Similar to that in Figures 6 and 7, the results with C_m in Equation (3) were better than C_m = 0.5. The trend of the three curves in Figure 13 was the same, that is, the velocity of the sphere impacting the ice plate was inversely proportional to the relative density. This is in line with our common sense. In Figures 14 and 15, with the increase of relative density, the kinetic energy and momentum of the sphere at the moment of impact both rose before they fell, and the trend was little-affected by the choice of C_m. As a result, there were two different relative densities that maximized the kinetic energy and momentum of the sphere, respectively. Because we tried to find an optimal dimensionless density $\bar{\rho}_{op}$ to break the ice plate the most, we needed to sort out the failure state of the ice plate impacted by the spheres with different relative densities.

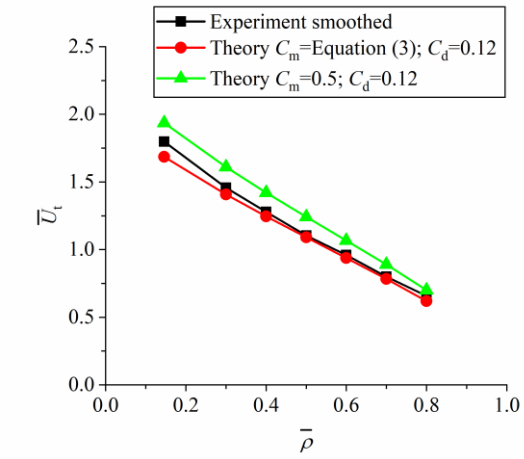

Figure 13. The dimensionless velocity of the sphere just before contacting the ice plate versus the relative density obtained by three methods with $\bar{h}$ = 0.089 and $\bar{L}_0$ = 2.31 constant.

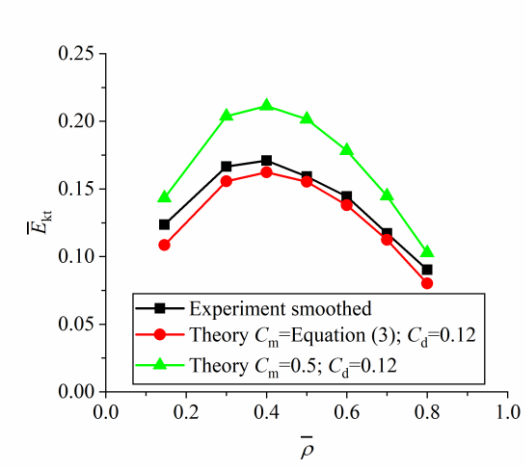

Figure 14. Dimensionless kinetic energy $\overline{E}_{kt}$ of the sphere just before contacting the ice plate versus the relative density obtained by three methods with $\overline{h}$ = 0.089 and $\overline{L}_0$ = 2.31 constant.

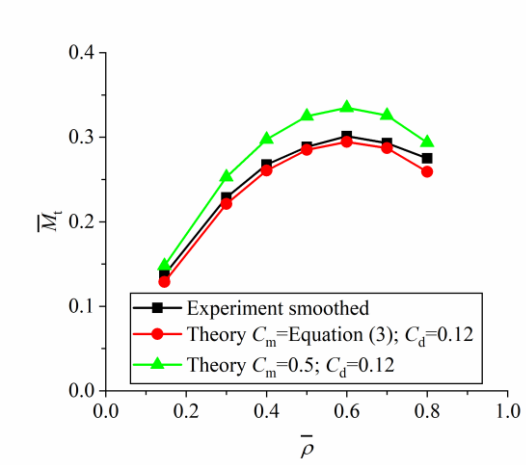

Figure 15. Dimensionless momentum $\overline{M}_t$ of the sphere just before contacting the ice plate versus the relative density obtained by three methods with $\overline{h}$ = 0.089 and $\overline{L}_0$ = 2.31 constant.

Figure 16 shows typical pictures of the damage on the ice plate caused by spheres of different densities, at t' = 0.1 s from a bird's-eye view and horizontal view, respectively. From Figure 16a–c, it can be seen that with the increase of the relative density of the sphere, the damage state of the ice plate changes from "debris splashing" to "ice plate breakup" patterns; while from Figure 16c–e, the damage state of the ice plate changes from "ice plate breakup" to "debris splashing" and then to "RCs" patterns.

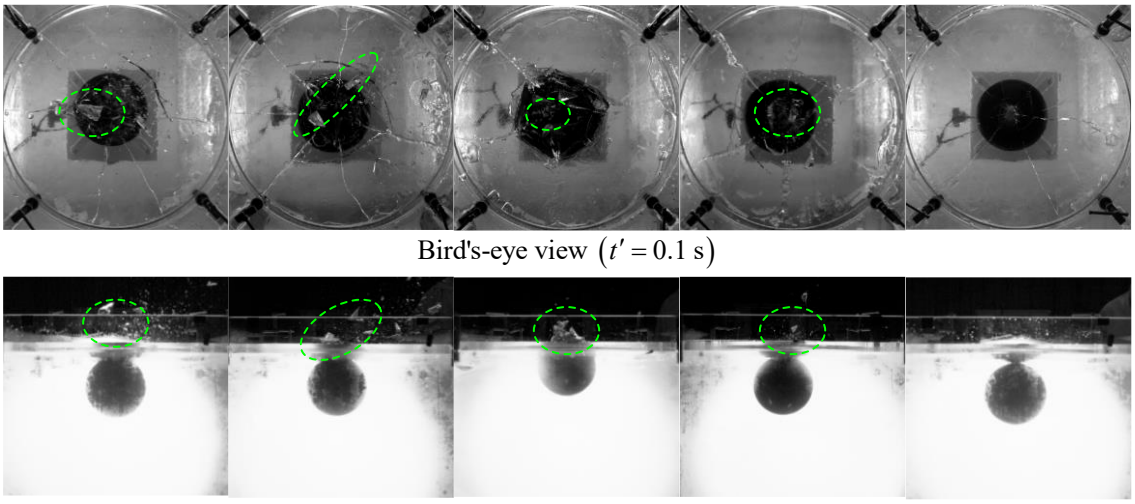

Figure 16. Destructiveness of ice plates caused by different relative densities of spheres $\bar{\rho}$, as denoted in the subfigures, from different views.

To avoid randomness in the results, at least 10 repeated experiments were done for each density case. The failure mode of the ice plate caused by spheres with different densities is shown in Figure 17. Because it was difficult to ensure that the properties of each ice plate were the same exactly due to the limits of icebreaking technology, different failure modes may appear at the same relative density. However, it was still reasonable to classify the damage degree of ice plates by statistical data of different failure modes.

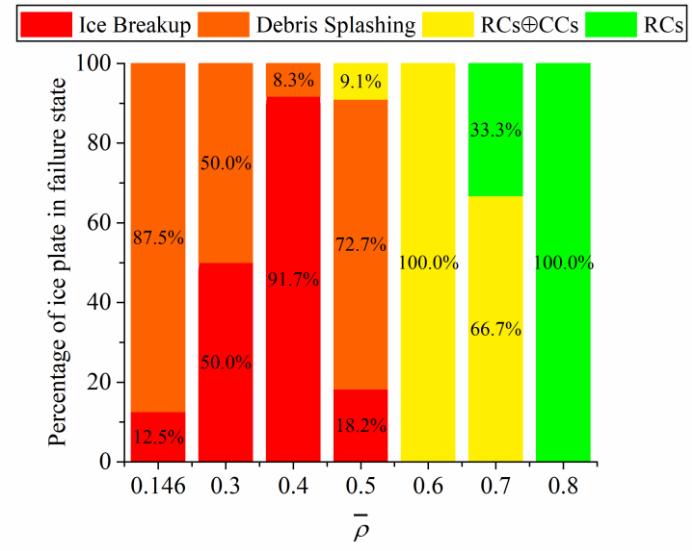

Figure 17. Probability of failure mode of ice plate impacted by spheres with different densities.

As discussed in Sections 4.3 and 4.4, the "ice plate breakup" pattern is the most severe of all the patterns. We took the probability of this pattern as a criterion and tried to link the damage degree of the ice plate with $\bar{E}_{kt}$ and $\bar{M}_t$ of the sphere in Figures 14 and 15. As shown in the Figure 18, the dimensionless kinetic energy of the sphere achieves the largest at $\bar{\rho}$ = 0.4, while the dimensionless momentum of the sphere achieves the largest at $\bar{\rho}$ = 0.6. Compared with the probability of the ice-breakup pattern, when the kinetic energy of the sphere is the largest, the probability of the ice plate breakup peaks (91.7%). From this

point, it can be concluded that the kinetic energy of the sphere, rather than momentum, at the moment of collision dominates the damage degree of the ice plate. As a result, we adopt kinetic energy of the sphere at the moment of collision as a criterion for the ice-breaking ability of a floating light sphere driven by net buoyant force hereinafter. This conclusion can also be well explained from the perspective of energy. When the sphere collided with the ice plate, the sphere converted its kinetic energy into kinetic and potential energies of the ice plate including cracks (or fracture energy), debris and fragments, kinetic and potential energies of fluid, the potential energy of the sphere as well as thermal energy [29]. The more kinetic energy the sphere gained before impact, the worse the ice plate was damaged (presenting in the generation of cracks, area of the hole, the motion of the debris and fragments, etc.).

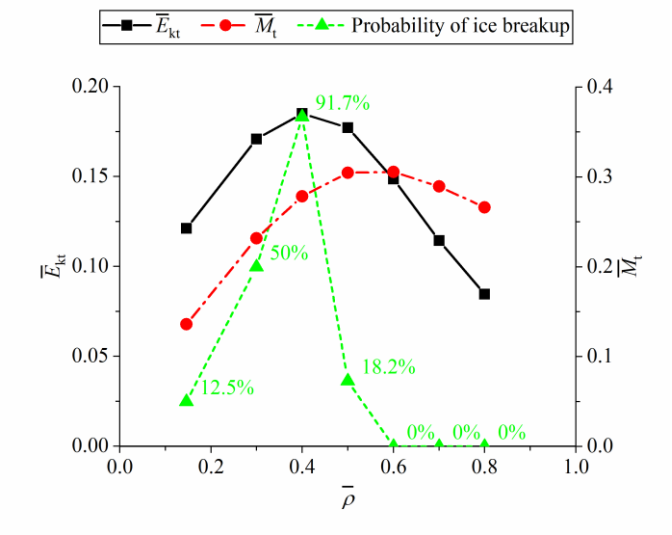

Figure 18. The relationship between $\overline{E}_{kt}$, $\overline{M}_t$ and the probability of the ice breakup with the relative density obtained in experiments.

We further plot the curve of $\overline{E}_{kt}$ versus $\overline{\rho}$ to find $\overline{\rho}_{op}$ with the case of $\overline{h} = 0.089$ and $\overline{L}_0 = 2.31$ in Figure 19. As mentioned above, considering that the added mass coefficient has little influence on the optimal density, we chose $C_m = 0.5$ as convenience and still chose $C_d = 0.12$ as before. It is clear that the theoretical optimal relative density $\overline{\rho}_{op} = 0.390$ was very close to the result in Figure 18 in the experiment. Therefore, when the initial depth $\overline{L}_0$ and ice thickness $\overline{h}$ were constant, one can predict the optimal relative density $\overline{\rho}_{op}$ in theory.

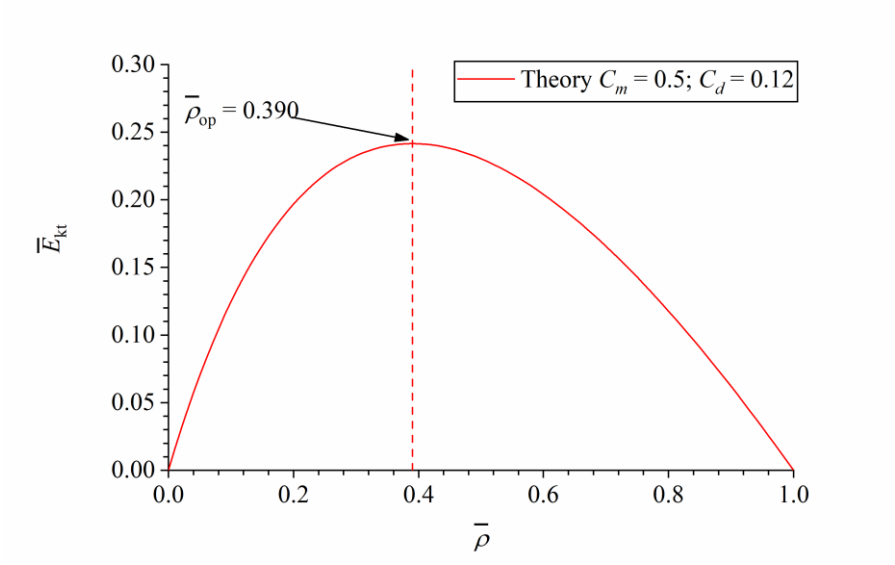

Figure 19. Dimensionless kinetic energy of the sphere versus dimensionless density of the sphere with $\bar{h} = 0.089$ and $\bar{L}_0 = 2.31$.

On the other hand, we further considered the relationship of $\bar{\rho}_{op}$ with $\bar{L}_0$ and C_d. First, we studied a simplified model with a non-viscous assumption, i.e., $C_d = 0$. Under this assumption, the dimensionless kinetic energy $\bar{E}_{kt}$ of the sphere can be obtained on the basis of Equation (8):

$$\bar{E}_{kt} = \frac{\pi}{3}\left(\bar{L}_0 - \frac{1}{2}\right)\cdot\bar{\rho}\left(\frac{1-\bar{\rho}}{1+2\bar{\rho}}\right). \tag{9}$$

$\bar{\rho}_{op}$ can be obtained by:

$$\frac{\partial \bar{E}_{kt}}{\partial \bar{\rho}} = \frac{\pi}{3}\left(\bar{L}_0 - \frac{1}{2}\right)\cdot\frac{1-2\bar{\rho}-2\bar{\rho}^2}{\left(1+2\bar{\rho}\right)^2} = 0\,, \tag{10}$$

$$\bar{\rho}_{op} = \frac{\sqrt{3}-1}{2} \approx 0.366\,. \tag{11}$$

Furthermore, for viscous assumption ($C_d \neq 0$), the dimensionless kinetic energy and its derivation with respect to $\bar{\rho}$ are

$$\bar{E}_{kt} = \frac{\bar{\rho}\pi}{12}\left(\bar{U}\right)^2 = \frac{\pi\bar{\rho}\left(1-\bar{\rho}\right)}{9C_d}\left[1 - e^{-\frac{3C_d}{(1+2\bar{\rho})}\left(\bar{L}_0-\frac{1}{2}\right)}\right], \tag{12}$$

$$\frac{\partial \bar{E}_{kt}}{\partial \bar{\rho}} = -\frac{\pi e^{-\frac{3C_d\left(\bar{L}_0-\frac{1}{2}\right)}{1+2\bar{\rho}}}\left\{1+\left[2+6C_d\left(\bar{L}_0-\frac{1}{2}\right)\right]\bar{\rho}-2\bar{\rho}^2\left[2+3C_d\left(\bar{L}_0-\frac{1}{2}\right)\right]-8\bar{\rho}^3\right\}}{9C_d\left(1+2\bar{\rho}\right)^2} + \frac{\pi\left(2\bar{\rho}-1\right)}{9C_d} = 0\,. \tag{13}$$

By solving Equation (13), one can obtain $\bar{\rho}_{op}$ with given $\bar{L}_0$ and C_d. As Equation (13) is complex and it is hard to obtain an explicit $\bar{\rho}_{op}$, we solved Equation (13) numerically. The relationship between $\bar{\rho}_{op}$ and $\bar{L}_0$ at different C_d is demonstrated in Figure 20.

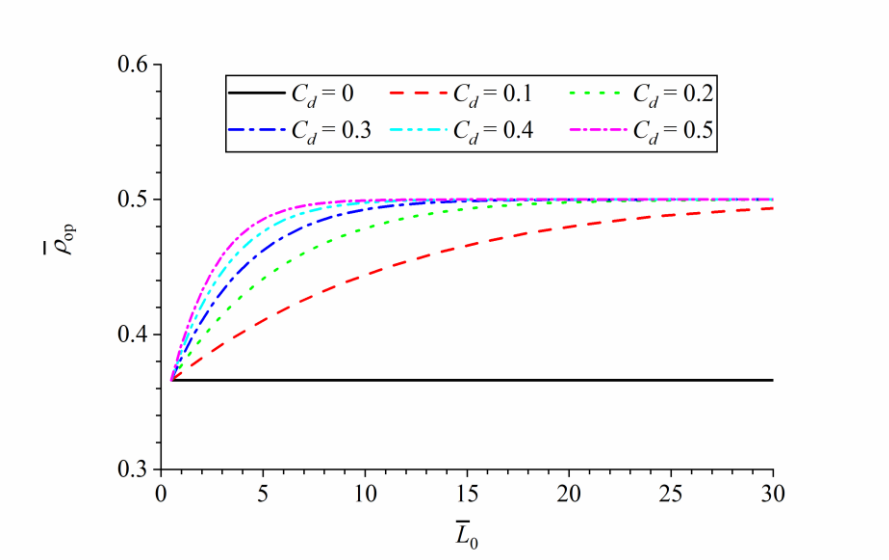

Figure 20. The relationship between $\bar{\rho}_{op}$ and $\bar{L}_0$ with different C_d.

According to Figure 20, one can find that no matter what $\bar{L}_0$ is, $\bar{\rho}_{op}$ is always not larger than 0.5. When considering the viscosity of water ($C_d \neq 0$), optimal relative density $\bar{\rho}_{op}$ of the sphere gradually approaches 0.5 with the increase of the initial depth $\bar{L}_0$. In fact, according to Equation (12), we can obtain the dimensionless kinetic energy of the sphere when the $\bar{L}_0$ approaches infinity:

$$\bar{E}_{kt(\bar{L}_0 \to \infty)} = \frac{\pi \bar{\rho}(1-\bar{\rho})}{9C_d}, \tag{14}$$

and $\bar{\rho}_{op}$ of this state can be obtained as

$$\bar{\rho}_{op(\bar{L}_0 \to \infty)} = 0.5, \tag{15}$$

which coincides well with the trend in Figure 20. By observing the curves with different C_d in Figure 20, one can find that $\bar{\rho}_{op}$ declines along with the decrease of C_d for a given $\bar{L}_0$. The smaller C_d is, the larger the initial depth $\bar{L}_0$ is required for $\bar{\rho}_{op}$ approaching to 0.5. When C_d is small enough but non-zero, it will need a very large initial depth for $\bar{\rho}_{op}$ approaching to 0.5. In other words, as long as the sphere moves in a viscous fluid (C_d is a constant), $\bar{\rho}_{op}$ increases with the initial depth $\bar{L}_0$ until it is infinitely close to 0.5.

On the contrary, when the sphere moves in a non-viscous fluid, $\bar{\rho}_{op}$ is not affected by the initial depth $\bar{L}_0$, which is constantly equal to $\frac{\sqrt{3}-1}{2}$. The jump of $\bar{\rho}_{op}$ at a very large $\bar{L}_0$ for viscous and non-viscous cases can be attributed to the properties of viscous force. As the viscous force is proportional to the square of the velocity, the acceleration of the sphere decreases as the velocity increases. The acceleration would infinitely approach zero and the velocity of the sphere approaches a stable value. By contrast, the sphere which moves in a non-viscous environment will always accelerate under the action of the combined force. Therefore, the state of motion of the sphere differs at a very large $\bar{L}_0$ for viscous and non-viscous cases. From another point of view, the effect of fluid viscosity on the motion of the sphere needs time, and as long as the time is large enough, it changes the motion of the sphere as well as $\bar{\rho}_{op}$ no matter how small C_d is, compared to the non-viscous case. This can also be validated from another phenomenon in Figure 20. When the

initial depth $\bar{L}_0$ tends to 0.5, i.e., $\left(\bar{L}_0 - \frac{1}{2}\right) \to 0$, all the optimal relative density $\bar{\rho}_{op}$ of the sphere in viscous cases tends to the counterpart of the non-viscous case, that is $\bar{\rho}_{op} \to \frac{\sqrt{3}-1}{2}$. This is because that the displacement of the sphere is too small for fluid viscosity to exert influence on the motion of the sphere.

5. Conclusions

Icebreaking by a free-rising sphere driven by its buoyance was studied in this paper. The main concern was determining when the light sphere breaks the ice plate the most severely, or the optimal relative density of the sphere. A set of indoor experimental devices were designed, and high-speed photography was adopted to record the whole process, including the free-rising of the sphere, the collision between the sphere and the ice plate, crack initiation and propagation as well as breakups of the ice plate. The failure mode of the ice plate caused by the impact and the influence of different parameters on the icebreaking ability of the sphere were explored. Conclusions were drawn as below:

1) Impacted by the free-rising buoyant sphere, the ice plate was broken. In some cases, a conical crevasse was formed under the reflected tensile wave at the top surface of the ice plate. A typical damage mode of the ice plate under this impact was 'radial cracks, circumferential cracks, debris splashing and ice plate breakup' in sequence. As a result, four damage patterns were concluded as "RCs", "RCs⊕CCs", "debris splashing" and "ice-plate breakup" patterns, with the damage degree of the ice plate rising;
2) Since it was impossible to directly measure the ice plate at the moment of impact of the sphere, we took the probability of the breakup of ice plate as a criterion and tried to link it with the kinetic energy and momentum of the sphere, which were two controversial parameters in determining the damage degree of ice. For the working conditions described in this paper, we found that when the kinetic energy of the sphere peaks at $\bar{\rho} = 0.4$, the probability of the ice plate breakup is the highest, which is 91.7%. It was found that the kinetic energy of the sphere, rather than momentum at the moment of collision, dominates the damage degree of the ice plate. The greater the kinetic energy of the sphere, the more severely the ice plate was damaged. It was considered that part of the kinetic energy of the sphere was transformed into the fracture energy of the ice plate as well as the kinetic and potential energies of ice debris and fragments;
3) The optimal density of the sphere $\bar{\rho}_{op}$ damaged the ice plate the most severely. $\bar{\rho}_{op}$ can be estimated by theoretical analysis of the kinetic energy of the sphere. It was found that $\bar{\rho}_{op}$ depends on the viscous effect of the fluid to a great extent. If the viscous effect is neglected, or for a non-viscous case, $\bar{\rho}_{op}$ equals to $\frac{\sqrt{3}-1}{2}$ (or 0.366) identically. Otherwise, $\bar{\rho}_{op}$ declines along with the decrease of C_d at a given $\bar{L}_0$, and rises along with the increase of $\bar{L}_0$ at a given C_d, approaching to 0.5 for a very large $\bar{L}_0$ in the end.

In the future, research on numerical modelling based on the interaction of ice, water and a buoyant sphere will be carried out. Furthermore, the effect of the boundary conditions of the ice plate will be studied, including free-floating boundary conditions, etc.

Author Contributions: Conceptualization, H.T. and B.-Y.N.; Data curation, H.T.; Funding acquisition, B.-Y.N. and Y.-Z.X.; Methodology, H.T, C.-X.Z. and B.-Y.N.; Resources, B.-Y.N. and S.-C.D.; Software, L.H.; Supervision, B.-Y.N.; Writing-original draft, H.T. and B.-Y.N.; Writing-review & editing, H.T., Z.L. and B.-Y.N. All authors have read and agreed to the published version of the manuscript.

Funding: This work is supported by the National Natural Science Foundation of China (Nos. 52192693, 52192690, 51979051, 51979056 and U20A20327), and the National Key Research and Development Program of China (2021YFC2803400), to which the authors are most grateful.

Institutional Review Board Statement: Not applicable.

Informed Consent Statement: Not applicable.

Data Availability Statement: There are no publicly available data for this study.

Conflicts of Interest: The authors declare no conflict of interest.

Nomenclature

Parameters

A	cross-sectional area;
C_d	drag coefficient;
C_{du}	drag coefficient for unsteady motion;
C_m	added-mass coefficient;
D	diameter of the sphere;
F_b	buoyant force;
F_d	drag force,
F_g	gravity force;
g	acceleration of gravity;
h	thickness of the ice plate;
L_0	initial submergence depth of the sphere;
m	mass of the sphere;
m_a	added mass of the sphere;
U	velocity of the sphere;
U_t	velocity of the sphere when it contacts the ice plate;
V	volume of the sphere;
x	displacement of the rising buoyant sphere;
ρ_s	density of the sphere;
ρ_w	density of water;

Dimensionless Parameters

$\bar{E}_{kt}$	dimensionless kinetic energy of the sphere just before contacting the ice plate;
$\bar{h}$	dimensionless thickness of the ice plate;
$\bar{l}$	dimensionless distance between the center of the sphere and the wall;
$\bar{L}_0$	dimensionless initial submergence depth of the sphere;
$\bar{M}_t$	dimensionless momentum of the sphere just before contacting the ice plate;
t'	initial time when the sphere just contacted the bottom surface of the ice plate;
$\bar{\rho}$	dimensionless density of the sphere;
$\bar{\rho}_{op}$	an optimal dimensionless density of the sphere to break the ice plate most

References

1. Thomson, J.; Rogers, W.E. Swell and sea in the emerging Arctic Ocean. *Geophys. Res. Lett.* **2014**, *41*, 3136–3140. https://doi.org/10.1002/2014gl059983.
2. Rogers, W.E.; Thomson, J.; Shen, H.H.; Doble, M.J.; Wadhams, P.; Cheng, S. Dissipation of wind waves by pancake and frazil ice in the autumn Beaufort Sea. *J. Geophys. Res. Oceans* **2016**, *121*, 7991–8007. https://doi.org/10.1002/2016jc012251.
3. Li, Z.; Ringsberg, J.W.; Rita, F. A voyage planning tool for ships sailing between Europe and Asia via the Arctic. *Ships Offshore Struct.* **2020**, *15*, S10–S19. https://doi.org/10.1080/17445302.2020.1739369.

4. Ni, B.-Y.; Han, D.-F.; Di, S.-C.; Xue, Y.-Z. On the development of ice-water-structure interaction. *J. Hydrodyn.* **2020**, *32*, 629–652. https://doi.org/10.1007/s42241-020-0047-8.
5. Zemlyak, V.; Pogorelova, A.; Kozin, V. Motion of a submerged body in a near-surface water environment. *Int. J. Nav. Arch. Ocean Eng.* **2021**, *14*, 100433. https://doi.org/10.1016/j.ijnaoe.2021.100433.
6. Cho, S.-R.; Lee, S. A prediction method of ice breaking resistance using a multiple regression analysis. *Int. J. Nav. Arch. Ocean Eng.* **2015**, *7*, 708–719. https://doi.org/10.1515/ijnaoe-2015-0050.
7. Huang, Y.; Sun, J.; Ji, S.; Tian, Y. Experimental study on the resistance of a transport ship navigating in level ice. *J. Mar. Sci. Appl.* **2016**, *15*, 105–111. https://doi.org/10.1007/s11804-016-1351-0.
8. Skripnuk, D.F.; Iliyushchenko, I.O.; Kulik, S.V.; Stepanova, M.M. Analysis of the current state of the Northern Sea Route and the potential development of the icebreaker fleet. *IOP Conf. Series Earth Environ. Sci.* **2020**, *539*, 012129. https://doi.org/10.1088/1755-1315/539/1/012129.
9. Zheng, X.; Tian, Z.; Xie, Z.; Zhang, N. Numerical Study of the Ice Breaking Resistance of the Icebreaker in the Yellow River Through Smoothed-Particle Hydrodynamics. *J. Mar. Sci. Appl.* **2022**, *21*, 1–14. https://doi.org/10.1007/s11804-022-00259-w.
10. Bukatov, A.E.; Zharkov, V.V. Influence of a floating elastic plate on the surface effects of internal waves generated by motion of a source in a non-homogeneous liquid. *Fluid Dyn.* **1995**, *30*, 254–260.
11. Zemlyak, V.L.; Kozin, V.M.; Baurin, N.O.; Petrosyan, G.V. Influence of Peculiarities of the Form of a Submarine Vessel on the Parameters of Generated Waves in the Ice Motion. In Proceedings of the 24th International Ocean and Polar Engineering Conference, Busan, Korea, 15–20 June 2014.
12. Pogorelova, A.V.; Zemlyak, V.L.; Kozin, V.M. Moving of a submarine under an ice cover in fluid of finite depth. *J. Hydrodyn.* **2018**, *31*, 562–569. https://doi.org/10.1007/s42241-018-0143-1.
13. de Graaf, K.L.; Penesis, I.A.; Brandner, P. Modelling of seismic airgun bubble dynamics and pressure field using the Gilmore equation with additional damping factors. *Ocean Eng.* **2014**, *76*, 32–39. https://doi.org/10.1016/j.oceaneng.2013.12.001.
14. Wu, Q.-G.; Wang, Z.-C.; Ni, B.-Y.; Yuan, G.-Y.; Semenov, Y.A.; Li, Z.-Y.; Xue, Y.-Z. Ice-Water-Gas Interaction during Icebreaking by an Airgun Bubble. *J. Mar. Sci. Eng.* **2022**, *10*, 1302. https://doi.org/10.3390/jmse10091302.
15. Yuan, G.-Y.; Ni, B.-Y.; Wu, Q.-G.; Xue, Y.-Z.; Han, D.-F. Ice breaking by a high-speed water jet impact. *J. Fluid Mech.* **2022**, *934*, A1. https://doi.org/10.1017/jfm.2021.999.
16. Ye, L.Y.; Guo, C.Y.; Wang, C.; Chang, X. Peridynamic solution for submarine surfacing through ice. *Ships Offshore Struct.* **2019**, *15*, 535–549. https://doi.org/10.1080/17445302.2019.1661626.
17. George, J.C.; Clark, C.; Carroll, G.M.; Ellison, W.T. Observations on the Ice-Breaking and Ice Navigation Behavior of Migrating Bowhead Whales (*Balaena mysticetus*) near Point Barrow, Alaska, Spring 1985. *Arctic* **1989**, *42*, 24–30. https://doi.org/10.14430/arctic1636.
18. Beltaos, S. Collapse of floating ice covers under vertical loads: Test data vs. theory. *Cold Reg. Sci. Technol.* **2002**, *34*, 191–207. https://doi.org/10.1016/s0165-232x(02)00004-6.
19. Kerr, A.D. The bearing capacity of floating ice plates subjected to static or quasi-static loads. *J. Glaciol.* **1976**, *17*, 229–268.
20. Shapiro, G.S. Design of a plate conceived as an infinite band resting upon elastic foundation. *Comptes Rendus De L'académie Des Sci. De l'URSS* **1942**, *37*, 202–204.
21. Timoshenko, S.; MacCullough, G.M. *Elements of Strength of Materials*; D. Van Nostrand: Toronto, Canada, 1940.
22. Assur, A. *Airfields on Floating Ice Sheets for Routine and Emergency Operations (Sipre Report, 36);* Corps of Engineers, U.S. Army, Snow Ice and Permafrost Research Establishment: Wilmette, IL, USA, 1956.
23. Frankenstein, G.E. *Load Test Data for Lake Ice Sheets*; U.S. Army Cold Regions Research and Engineering Laboratory: Wilmette, IL, USA, 1963.
24. Field, J.E. ELSI conference: Invited lecture: Liquid impact: Theory, experiment, applications. *Wear* **1999**, *233*, 1–12. https://doi.org/10.1016/s0043-1648(99)00189-1.
25. Bowden, F.P.; Brunton, J.H. The deformation of solids by liquid impact at supersonic speeds. *Proc. R. Soc. London Ser. A, Math. Phys. Sci.* **1961**, *263*, 433–450. https://doi.org/10.1098/rspa.1961.0172.
26. Bouzid, S.; Nyoungue, A.; Azari, Z.; Bouaouadja, N.; Pluvinage, G. Fracture criterion for glass under impact loading. *Int. J. Impact Eng.* **2001**, *25*, 831–845. https://doi.org/10.1016/s0734-743x(01)00023-9.
27. Zhang, Y.; Wang, Q.; Han, D.; Xue, Y.; Lu, S.; Wang, P. Dynamic splitting tensile behaviours of distilled-water and river-water ice using a modified SHPB setup. *Int. J. Impact Eng.* **2020**, *145*, 103686. https://doi.org/10.1016/j.ijimpeng.2020.103686.
28. Woodward, R.L.; Baxter, B.J.; Pattie, S.D.; McCarthy, P. Impact fragmentation of brittle materials. *Le J. Phys. Colloq.* **1991**, *1*, C3–C259. https://doi.org/10.1051/jp4:1991336.
29. Dooge, D.; Singh, S.; Masiulaniec, K.; Dewitt, K. Experimental assessment of airframe damage due to impacting ice. In Proceedings of 31st Aerospace Sciences Meeting, Reno, NV, USA, 11–14 January 1993.
30. Kim, H.; Welch, D.A.; Kedward, K.T. Experimental investigation of high velocity ice impacts on woven carbon/epoxy composite panels. *Composites, Part A* **2003**, *34*, 25–41.
31. Carney, K.S.; Benson, D.J.; DuBois, P.; Lee, R. A phenomenological high strain rate model with failure for ice. *Int. J. Solids Struct.* **2006**, *43*, 7820–7839. https://doi.org/10.1016/j.ijsolstr.2006.04.005.
32. Combescure, A.; Chuzel-Marmot, Y.; Fabis, J. Experimental study of high-velocity impact and fracture of ice. *Int. J. Solids Struct.* **2011**, *48*, 2779–2790. https://doi.org/10.1016/j.ijsolstr.2011.05.028.

33. Pernas-Sánchez, J.; Pedroche, D.A.; Varas, D.; López-Puente, J.; Zaera, R. Numerical modeling of ice behavior under high velocity impacts. *Int. J. Solids Struct.* **2012**, *49*, 1919–1927. https://doi.org/10.1016/j.ijsolstr.2012.03.038.
34. Xue, L.; Coble, C.R.; Lee, H.; Yu, D.; Chaparala, S.; Park, S. Dynamic analysis of thin glass under ball drop impact with new metrics. In Proceedings of International Electronic Packaging Technical Conference and Exhibition, Garden Grove, CA, USA, 16–18 July 2013.
35. Knut, A.; Ocaña Atencio, R.E.; Sandig, F.; Pankrath, H.; Thiele, R.; Kirstein, J. Influence of the momentum and the energy on the performance of dynamic compaction technologies–recent field and laboratory tests. In Proceedings of the XVII European Conference on Soil Mechanics and Geotechnical Engineering, Reykjavik, Iceland, 1–7 September 2019.
36. Kozlov, D. Mathematical model of transverse impact of a solid spherical body on the ice cover surface, In Proceedings of the 3rd International Scientific Conference on Polar Mechanics, Vladivostok, Russia, 27–30 September 2016; pp. 115–122.
37. Orlov, M.; Bogomolov, G. Study of the behavior of ice under shock and explosive loading. In Proceedings of the 3rd In-ternational Scientific Conference on Polar Mechanics, Vladivostok, Russia, 27–30 September 2016; pp. 192–202.
38. Ren, H.; Zhao, X. Numerical simulation for ice breaking and water entry of sphere. *Ocean Eng.* **2021**, *243*, 110198. https://doi.org/10.1016/j.oceaneng.2021.110198.
39. Wang, C.; Wang, J.; Wang, C.; Guo, C.; Zhu, G. Research on vertical movement of cylindrical structure out of water and breaking through ice layer based on S-ALE method. *J. Theor. App. Mech. Pol.* **2021**, *53*, 3110–3123.
40. Batchelor, C.K. *An Introduction to Fluid Dynamics*; Cambridge University Press: Cambridge, UK, 2000.
41. Ni, B.Y.; Wu, G.X. Numerical simulation of water exit of an initially fully submerged buoyant spheroid in an axisymmetric flow. *Fluid Dyn. Res.* **2017**, *49*, 045511. https://doi.org/10.1088/1873-7005/aa747b.
42. Semenov, Y.A. Nonlinear flexural-gravity waves due to a body submerged in the uniform stream. *Phys. Fluids* **2021**, *33*, 052115. https://doi.org/10.1063/5.0048887.
43. Kharlamov, A.A.; Chára, Z.; Vlasak, P. Hydraulic formulae for the added masses of an impermeable sphere moving near a plane wall. *J. Eng. Math.* **2007**, *62*, 161–172. https://doi.org/10.1007/s10665-007-9186-y.
44. Egorov, A.I. *Riccati Equations (Russian Academic Monographs)*; Pensoft Publishers: Moscow, Russia, 2007; Volume 5.
45. Gold, L.W. Engineering Properties of Fresh-Water Ice. *J. Glaciol.* **1977**, *19*, 197–212. https://doi.org/10.3189/s0022143000215608.
46. Schulson, E.M. The structure and mechanical behavior of ice. *Jom* **1999**, *51*, 21–27. https://doi.org/10.1007/s11837-999-0206-4.
47. Timco, G.W.; Weeks, W.F. A review of the engineering properties of sea ice. *Cold Reg. Sci. Technol.* **2010**, *60*, 107–129. https://doi.org/10.1016/j.coldregions.2009.10.003.
48. Michel, B.; Ramseier, R.O. Classification of river and lake ice. *Can. Geotech. J.* **1971**, *8*, 36–45. https://doi.org/10.1139/t71-004.
49. Ashton, G.D. *River and Lake Ice Engineering*, 2nd ed.; Water Resources Publications: Lansing, MI, USA, 1986; pp. 166–174.
50. Rogozhnikova, E.G.; Kozin, V.M.; Zemlyak, V.L. Experimental Studies of Influence of the Distance between Loads on the Nature of Destruction of an Ice Cover when Paired Loads are Moving over the Ice Cover. In Proceedings of the 29th International Ocean and Polar Engineering Conference, Honolulu, HI, USA, 16–21 June 2019.
51. Murdza, A.; Schulson, E.M.; Renshaw, C.E. Strengthening of columnar-grained freshwater ice through cyclic flexural loading. *J. Glaciol.* **2020**, *66*, 556–566. https://doi.org/10.1017/jog.2020.31.
52. Chen, S.; Gad, E.; Zhang, L.; Lam, N.; Xu, S.; Lu, G. Experiments on an ice ball impacting onto a rigid target. *Int. J. Impact Eng.* **2022**, *167*, 104281. https://doi.org/10.1016/j.ijimpeng.2022.104281.
53. Ni, B.Y.; Pan, Y.T.; Yuan, G.Y.; Xue, Y.Z. An experimental study on the interaction between a bubble and an ice floe with a hole. *Cold Reg. Sci. Technol.* **2021**, *187*, 103281. https://doi.org/10.1016/j.coldregions.2021.103281.
54. Krishnaiyar, N.C. CXI. An Experimental Determination of the Inertia of a Sphere Vibrating in a Liquid. *Lond. Edinb. Dublin Philos. Mag. J. Sci.* **1923**, *46*, 1049–1053. https://doi.org/10.1080/14786442308634332.
55. Odar, F.; Hamilton, W.S. Forces on a sphere accelerating in a viscous fluid. *J. Fluid Mech.* **1964**, *18*, 302–314. https://doi.org/10.1017/s0022112064000210.
56. Mei, R. Flow due to an oscillating sphere and an expression for unsteady drag on the sphere at finite Reynolds number. *J. Fluid Mech.* **1994**, *270*, 133–174. https://doi.org/10.1017/s0022112094004222.
57. Karanfilian, S.K.; Kotas, T.J. Drag on a sphere in unsteady motion in a liquid at rest. *J. Fluid Mech.* **1978**, *87*, 85–96. https://doi.org/10.1017/s0022112078002943.
58. Schlichting, H.; Kestin, J. *Boundary Layer Theory*, 9th ed.; Springer: New York, NY, USA, 1961.
59. Bird, R.B.; Stewart, W.E.; Lightfoot, E.N. *Transport Phenomena*, 2nd ed.; Wiley: John Wiley & Sons, USA, 2012.
60. Morrison, F.A. *Data Correlation for Drag Coefficient for Sphere*; Department of Chemical Engineering, Michigan Technological University: Houghton, MI, USA, 2013; p. 49931.
61. Perry, R.H.; Chilton, C.H. *Perry's Chemical Engineers' Handbook*, 5trh ed.; McGraw-Hill: Kogakusha, Tokyo, 1973.
62. Temkin, S.; Kim, S.S. Droplet motion induced by weak shock waves. *J. Fluid Mech.* **1980**, *96*, 133–157. https://doi.org/10.1017/s0022112080002054.
63. Temkin, S.; Mehta, H.K. Droplet drag in an accelerating and decelerating flow. *J. Fluid Mech.* **1982**, *116*, 297–313. https://doi.org/10.1017/s0022112082000470.

64. Bowden, F.P.; Field, J.E. The brittle fracture of solids by liquid impact, by solid impact, and by shock. *Proc. R. Soc. London Ser. A, Math. Phys. Sci.* **1964**, *282*, 331–352. https://doi.org/10.1098/rspa.1964.0236.
65. Bazant, Z.P.; Kim, J.J.H.; Li, Y.N. Part-through bending cracks in sea ice plates: Mathematical modeling. *J. Appl Mech. T ASME* **1995**, *207*, 97–105.

Disclaimer/Publisher's Note: The statements, opinions and data contained in all publications are solely those of the individual author(s) and contributor(s) and not of MDPI and/or the editor(s). MDPI and/or the editor(s) disclaim responsibility for any injury to people or property resulting from any ideas, methods, instructions or products referred to in the content.

https://dspace.org/

When does a light sphere break ice plate most by using its net buoyance?

Ni, Bao-Yu; Tan, Hao; Di, Shao-Cheng; Zhang, Chen-Xi; Li, Zhiyuan ...

2023-02-01
MDPI
https://doi.org/10.3390/jmse11020289
Ni BY, Tan H, Di SC, et al., (2023) When does a light sphere break ice plate most by using its net buoyance?. Journal of Marine Science and Engineering, Volume 11, Issue 2, February 2023, Article number 289

Downloaded from a DSpace repository. https://dspace.org/